

Influence of Meso and Nanoscale Structure on the Properties of Highly Efficient Small Molecule Solar Cells

Tobias Moench, Pascal Friederich, Felix Holzmueller, Bogdan Rutkowski, Johannes Benduhn, Timo Strunk, Christian Koerner, Koen Vandewal, Aleksandra Czyrska-Filemonowicz, Wolfgang Wenzel, and Karl Leo*

The nanoscale morphology of the bulk heterojunction absorber layer in an organic solar cell (OSC) is of key importance for its efficiency. The morphology of high performance vacuum-processed, small molecule OSCs based on oligothiophene derivatives (DCV5T-Me) blended with C₆₀ on various length scales is studied. The analytical electron microscopic techniques such as scanning transmission electron microscopy, energy dispersive X-ray spectroscopy, highly sensitive external quantum efficiency measurements, and meso and nanoscale simulations are employed. Unique insights into the relation between processing, morphology, and efficiency of the final devices are obtained. It is shown that the connectivity of the oligothiophene-C₆₀ network is independent of the material domain size. The decisive quantity controlling the internal quantum efficiency is the energetic disorder induced by material mixing, strongly limiting charge and exciton transport in the OSCs.

1. Introduction

Organic solar cells (OSCs) have the potential to contribute to the future demand for renewable electrical energy due to low material consumption, low weight, and other favorable properties.^[1] These specific advantages of OSCs allow various innovative applications such as building- or clothing-integrated photovoltaics.^[2] Today's most efficient organic solar cells are based on small molecules, reaching efficiencies >9% in single-junction and up to 12% in tandem devices.^[3,4]

T. Moench, F. Holzmueller, J. Benduhn, Dr. C. Koerner,
Prof. K. Vandewal, Prof. K. Leo
Institut für Angewandte Photophysik
TU Dresden
George-Bähr-Strasse 1, 01062 Dresden, Germany
E-mail: karl.leo@iapp.de

P. Friederich, Prof. W. Wenzel
Institut für Nanotechnologie
Karlsruher Institut für Technologie
Hermann-von-Helmholtz-Platz 1
76344 Eggenstein-Leopoldshafen, Germany

Dr. B. Rutkowski, Prof. A. Czyrska-Filemonowicz
International Centre of Electron Microscopy for Materials Science
AGH University of Science and Technology
Al. Mickiewicza 30, 30-059 Kraków, Poland

Dr. T. Strunk
Nanomatch GmbH
Hermann-von-Helmholtz-Platz 1
76344 Eggenstein-Leopoldshafen, Germany

To further improve the power conversion efficiencies (PCEs) of OSCs, it is necessary to understand the complicated photon-to-electron conversion processes in detail. One important challenge is to understand the relationship between controlled processing of high-performance OSCs, the resulting nanoscopic morphology of the absorber layer, and subsequent PCE of the completed device. This multiscale problem can be only tackled by thoroughly characterizing the different length scales, from the sub-nanometer to the centimeter scale, and complementary simulations to obtain comprehensive insight into the microscopic processes involved in every step.^[5-7]

At the heart of a bulk heterojunction (BHJ) OSC is a blend of two or more organic materials forming the absorber layer of the solar cell.^[5,6] The advantage of this blend architecture over a bilayer structure lies in the increased interfacial area between donor and acceptor materials, which increases the dissociation probability of the strongly bound photogenerated exciton (Frenkel exciton). Once separated into free charge carriers at the material interface, the morphology of the blend layer must provide closed transport paths to the adjacent layers for charge extraction. Thus, the solar cell efficiency is highly sensitive to the size and connectivity of a phase to its adjacent layer, as well as the material purity of each domain.^[7,8] Overall, the constraints for an optimal morphology are manifold, requiring a sufficiently fine-grained morphology for efficient exciton dissociation, but still sufficiently coarse for an unhampered charge carrier transport. Hence, the BHJ of an efficient OSC requires a morphology balancing these competing demands. A powerful method to adjust the BHJ morphology in vacuum processed small molecule based OSCs is to control the substrate temperature (T_{sub}) during deposition of the absorber layer.^[9-12] In this contribution, we study the relationship between T_{sub} , nanoscopic morphology of the BHJ and PCE of the final OSC, with both experimental and theoretical methods.

We fabricated and characterized BHJ OSCs, where the intrinsic absorber layer is sandwiched between n-doped and p-doped layers (nip OSC) to ensure an unhampered charge transport to the respective contacts.^[13] The intrinsic BHJ absorber layer of such nip OSCs is composed of the dicyanovinyl-substituted oligothiophene derivative DCV5T-Me

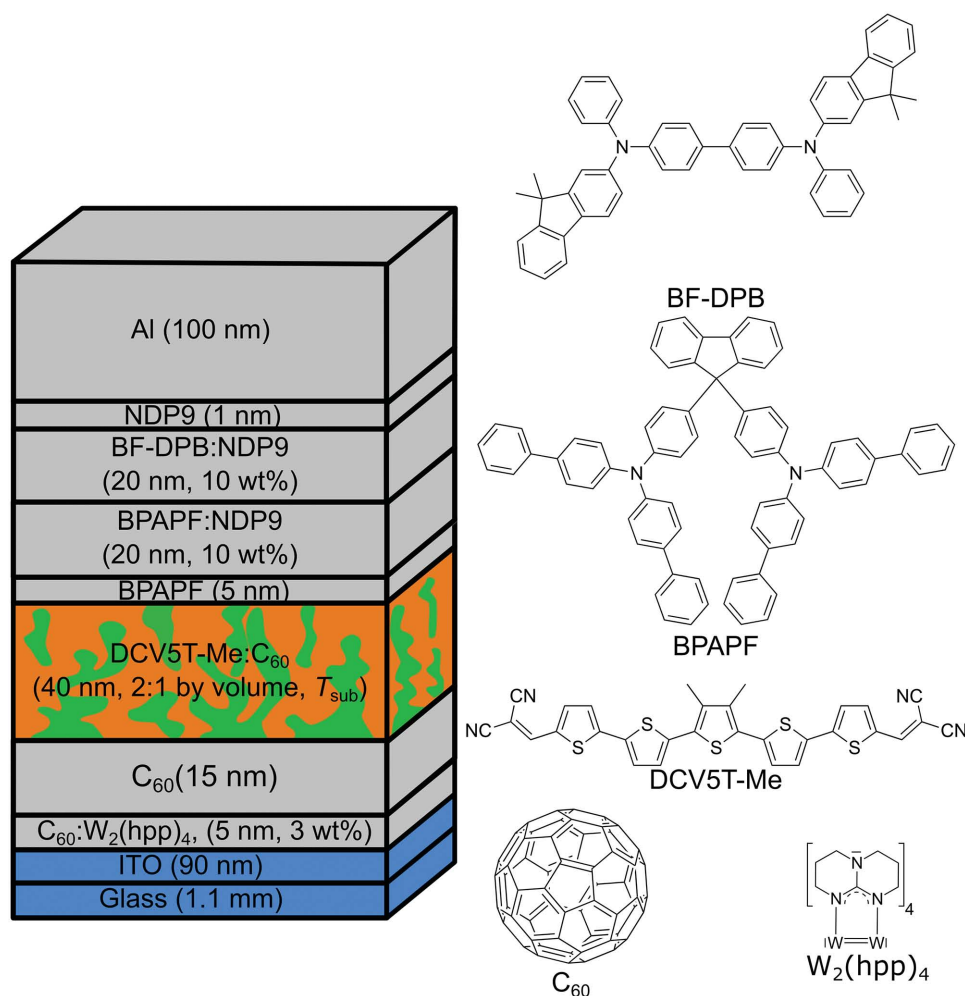


Figure 1. Layer sequence of the investigated OSCs and the corresponding molecular structures of its compounds. DCV5T-Me and C₆₀ constitute the absorber layer. For this study, they have been deposited at various substrate temperatures T_{sub} . The absorber layer is sandwiched between an electron conducting C₆₀ layer and a hole conducting BPAPF layer. To place the absorber layer in the optical field maximum, optically transparent, highly conductive n-doped (C₆₀:W₂(hpp)₄) and p-doped (BPAPF:NDP9 and BF-DPB:NDP9) layers are attached.

as donor and the fullerene C₆₀ as acceptor (see **Figure 1**).^[11,14–19] With this material system, calibrated PCEs of 8.3% were recently achieved.^[20]

To analyze the various BHJ absorber layer morphologies created by different substrate temperatures during material deposition, we utilized a scanning transmission electron microscope (STEM) equipped with a high-angle annular dark field (HAADF) and energy dispersive X-ray (EDX) detector.^[21] Hence, we are able to study the phase separation by means of chemical contrast at relevant nanoscopic length scales.^[22,23] To compare changes in the effective interface area upon substrate heating, we used sensitive external quantum efficiency (sEQE) measurements.^[24]

Subsequently, the experimental findings from the STEM-EDX images are used in microscopic and mesoscopic models to obtain 3D morphologies of the donor–acceptor blend, allowing for a straightforward interpretation of the current–voltage (j – V) curves in terms of microscopic parameters such as exciton migration, percolation paths, etc. We show that energetic disorder is the limiting parameter, determining the

efficiency of organic solar cells instead of donor and acceptor domain sizes.

2. Results

2.1. Device Characterization

Three OSCs were prepared with the layer sequence shown in **Figure 1**. For device A, the DCV5T-Me:C₆₀ absorber layer was deposited at room temperature (RT). The absorber layers of devices B and C at $T_{\text{sub}} = 80\text{ °C}$ and $T_{\text{sub}} = 140\text{ °C}$, respectively. The j – V characteristics of the respective OSCs were recorded with a mismatch corrected illumination to achieve AM1.5 equivalent conditions. The recorded j – V curves are presented in **Figure 2a** and the extracted solar cell parameters in **Table 1**.

The j – V characteristics reveal that moderate substrate heating improves the device performance. The fill factor (FF) increases from 43% to 57%, which is a clear indication for an enhanced charge carrier extraction. The short-circuit current

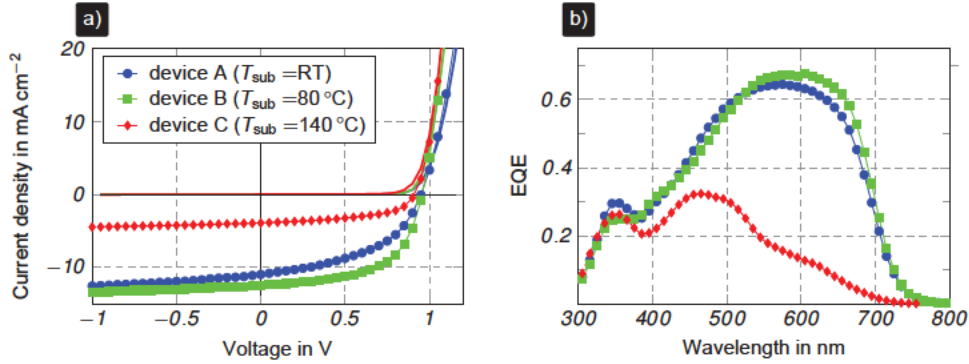


Figure 2. a) j - V curves of devices A (blue squares, BHJ deposited at room temperature), B (green circles, BHJ deposited at $T_{\text{sub}} = 80$ °C), and C (red triangles, BHJ deposited at $T_{\text{sub}} = 140$ °C) measured under mismatch corrected illumination intensity of 100 mW cm^{-2} . The solid lines without symbols show the dark j - V curves. b) Spectrally resolved EQEs of the same devices.

density (j_{sc}) increases from 10.9 mA cm^{-2} to 12.4 mA cm^{-2} . Figure 2b shows that the additional current density originates mainly from an increased EQE in the absorption range of DCV5T-Me around 590 nm. In combination with a slightly increased V_{oc} , the PCE rises significantly from 4.5% for device A to 6.8% for device B.

Increasing the substrate deposition temperature to $T_{\text{sub}} = 140$ °C decreases the solar cell performance. The contribution of DCV5T-Me to the EQE spectrum is reduced by 79% from the maximal EQE at 590 nm of 0.73 for device B to 0.15 for device C, reducing j_{sc} to 3.9 mA cm^{-2} . C_{60} generates the main contribution to j_{sc} , which is clearly visible in the EQE spectrum in the range from 300 to 450 nm. Together with reduced V_{oc} and FF, the PCE for device C is below that of device A at 1.9%.

2.2. Absorber Layer Morphology

To obtain insight into the absorber blend layer morphology, we utilized STEM-HAADF and STEM-EDX, where the HAADF signal corresponds to thickness variations, and the EDX signal arises from chemical contrast between DCV5T-Me and C_{60} . In a scanning transmission electron microscope, the electron beam is tightly focused to form a probe small enough to image atomic columns.^[21,25] Scanning across the sample and collecting the electrons scattered to angles $>3^\circ$ by a ring-shaped HAADF detector provides information on the material distribution (depending on the average atomic number of the probed material, rendering an effective Z-contrast). Since both C_{60} and DCV5T-Me predominantly consist of carbon, the contrast in

Table 1. j - V characteristics of devices A to C recorded under a mismatch corrected intensity of 100 mW cm^{-2} . Each value is the arithmetic average of eight devices produced on one wafer. Note that the measurement uncertainty of V_{oc} is $< 10 \text{ mV}$.

Device- T_{sub}	V_{oc} [V]	j_{sc} [mA cm^{-2}]	FF [%]	PCE [%]
A - RT	0.95	10.9 ± 0.08	43 ± 3	4.5 ± 0.3
B - 80 °C	0.96	12.4 ± 0.05	57 ± 0.7	6.8 ± 0.09
C - 140 °C	0.91	3.9 ± 0.04	43 ± 0.5	1.9 ± 0.02

HAADF images of the DCV5T-Me: C_{60} blend reflects thickness variations. Moreover, the impinging electrons can excite electrons from the inner shell of atoms. The corresponding relaxation of an electron originating from an outer shell leads to the emission of an X-ray photon. The emitted photons are simultaneously collected by an EDX detector and enable chemical contrast in STEM-EDX measurements.^[22,26,27] For the elemental quantification in STEM-EDX, we chose carbon (present in both DCV5T-Me and C_{60}) and sulfur (present only in DCV5T-Me). Note that STEM-EDX shows the quantitative mapping of domain purity in real space and is thus complementary to reciprocal space methods such as R-SoXS.^[7]

Figure 3a shows the HAADF signal of the DCV5T-Me: C_{60} (40 nm thickness, 2:1 by volume) blend deposited at $T_{\text{sub}} = \text{RT}$. Small round shaped structures generate a slightly higher HAADF signal compared to the rest of the sample. These bright structures are slightly thicker than the rest of the sample.

The STEM-EDX images of the carbon and sulfur content in the same sample are displayed in Figure 3b,c, respectively, showing a homogeneous mixture of DCV5T-Me and C_{60} . Therefore, we can conclude that the moderate short-circuit current density and PCE of the RT devices is related to a finely intermixed blend morphology of the absorber layer.

Figure 4 depicts the thin-film morphology of the absorber layer deposited at $T_{\text{sub}} = 80$ °C. The STEM-HAADF image (Figure 4a) appears homogeneous, indicating again the overall relatively low HAADF-contrast in this organic blend layer, apart from the relatively large bright structure at the bottom, which can be identified in the carbon map as a C_{60} -rich agglomerate.

The STEM-EDX images (Figure 4b,c) provide clear contrast between DCV5T-Me and C_{60} , revealing the morphology of the absorber layer. Here, we observe small carbon-rich islands (diameter $\approx 10 \text{ nm}$; Figure 4b), embedded in a well-connected sulfur-rich network (Figure 4c). Images recorded at lower magnifications, showing the large-scale character of this well-connected structure, can be found in Figure S2 (Supporting Information).

The phase separation of the absorber layer accompanied by an increased domain purity compared to the sample deposited at RT correlates well with the increased short-circuit current density and fill-factor of the OSC, providing a beneficial trade-off between closed pathways for the charge transport to the

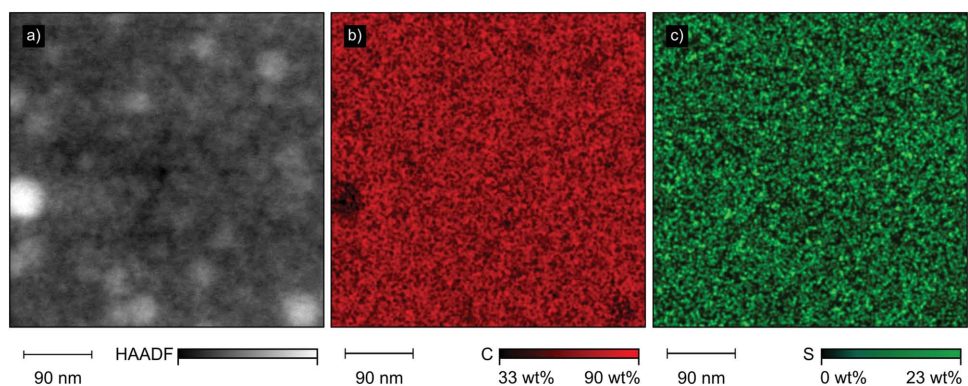


Figure 3. STEM images of a DCV5T-Me:C₆₀ blend layer deposited at $T_{\text{sub}} = \text{RT}$. The STEM-HAADF image a) shows small thickness variations of the DCV5T-Me:C₆₀ sample, whereas the STEM-EDX images b) and c) show the quantitative elemental distribution of carbon and sulfur indicating C₆₀ and DCV5T-Me-rich areas.

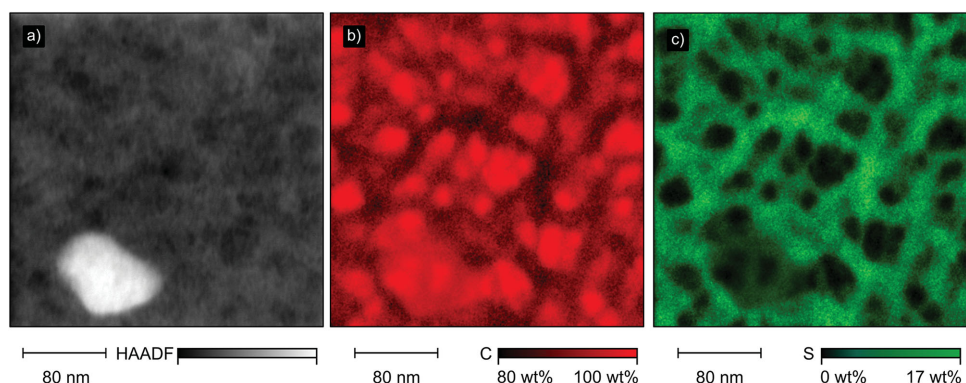


Figure 4. STEM images of DCV5T-Me:C₆₀ deposited at $T_{\text{sub}} = 80\text{ }^{\circ}\text{C}$. The STEM-HAADF image a) is indicating an overall homogeneous sample thickness. The STEM-EDX images depicted in b) and c) show small C₆₀ rich domains in a well-connected DCV5T-Me enriched network.

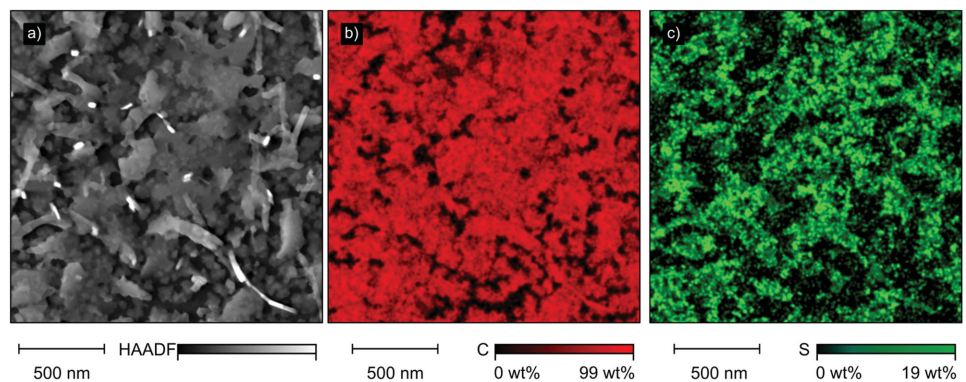


Figure 5. STEM images of DCV5T-Me:C₆₀ deposited at $T_{\text{sub}} = 140\text{ }^{\circ}\text{C}$. The STEM-HAADF image a) indicates strong thickness variations. The STEM-EDX images b) and c) show dark spots of 0 wt% material content, indicating an incomplete substrate coverage as well as disadvantageous phase separation of the constituents. Note the larger scale bar as compared to Figure 4.

respective electrodes and sufficient donor–acceptor-interface for exciton dissociation.

Increasing the substrate temperature during absorber layer deposition to $T_{\text{sub}} = 140\text{ }^{\circ}\text{C}$ results in a decreased solar cell PCE. The STEM-HAADF image (Figure 5a) indicates large thickness fluctuations. A large surface roughness of the absorber layers

is disadvantageous for a solar cell because it induces increased shunting of the device. Furthermore, the induced light scattering complicates the optical optimization of the device by means of transfer-matrix methods, possibly placing the absorber layer outside the optical field maximum. Moreover, the STEM-EDX images (Figure 5b,c) indicate a disadvantageous, large-area

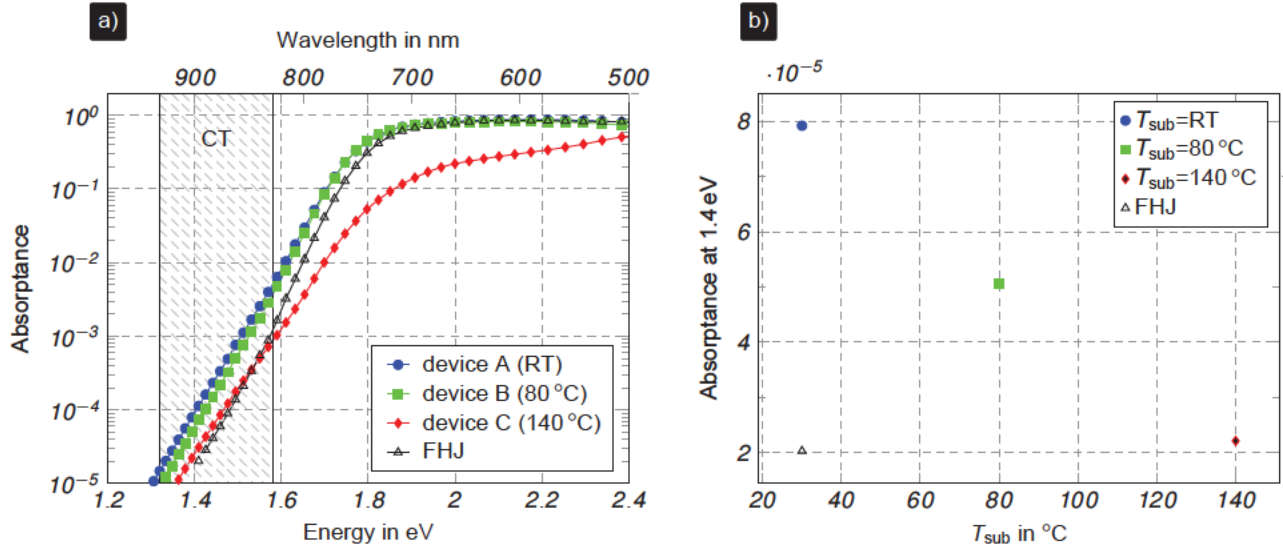


Figure 6. a) Energy resolved absorbance spectra $A(E)$ for the devices A to C and a flat heterojunction (FHJ) obtained by a sensitive EQE measurement. Part b) shows the substrate temperature dependence of the absorbance at 1.4 eV for the different devices.

demixing of DCV5T-Me and C_{60} compared to the sample prepared at $T_{\text{sub}} = 80^\circ\text{C}$. Additionally, we observe coinciding black regions (0 wt% for S and C) in Figure 5b, indicating an incomplete coverage of the substrate.

The strong demixing and the nonclosed layer formation at $T_{\text{sub}} = 140^\circ\text{C}$ in conjunction with the EQE spectrum shown in Figure 2b explains the breakdown of the solar cell efficiency: Partial substrate coverage lowers the amount of absorbed light in the absorber layer and, therefore, reduces the photon-to-electron conversion efficiency of the photons absorbed by DCV5T-Me.

Additionally, we performed sEQE measurements to investigate relative changes in the DCV5T-Me: C_{60} interface area of the devices A to C (see the Experimental section). At the low energy edge of the EQE spectrum (see Figure 2b), the photocurrent is generated by interfacial charge transfer (CT) state transitions, occurring at the interface between donor and acceptor. The strength of this absorption is, therefore, a measure of the interfacial area in the blend.

Figure 6a shows the absorbance spectra obtained by rescaling the sEQE spectra of devices A to C (see the Experimental Section). As a reference, the spectrum of a DCV5T-Me/ C_{60} bilayer (flat heterojunction, FHJ) is added in Figure 6a. Absorption in the spectral region between 1.3 and 1.5 eV is lowest in the bilayer device, which contains significantly less interface than the BHJ devices.

Figure 6b shows the absorbance at 1.4 eV over the substrate temperature T_{sub} . We observe a gradual decrease of interfacial area between donor and acceptor with increasing substrate temperature. At $T_{\text{sub}} = 80^\circ\text{C}$, the number of donor-acceptor contacts is reduced by approximately one third relative to the RT sample. Thus, this demixing of donor and acceptor ensures an optimal balance between exciton dissociation and charge carrier migration via closed transport paths. Increasing the substrate temperature to $T_{\text{sub}} = 140^\circ\text{C}$ reduces the number of donor-acceptor contacts, which is another contribution to the breakdown of the PCE.

2.3. Simulations

To link microscopic images and macroscopic j - V characteristics, EQE, and sEQE measurements, we utilized simulations aiming at better understanding the microscopic and mesoscopic mechanism of light-to-energy conversion in the DCV5T-Me: C_{60} OSCs. In the usually discussed working principle of OSCs, strongly bound excitons are generated in the bulk-heterojunction and migrate until they reach a material interface or decay to the ground state. At the interface, excitons dissociate with a certain probability into CT states, where the electron is localized on a C_{60} molecule and the hole on a DCV5T-Me molecule. Once the CT states are separated, the resulting charge carriers move towards the electrodes. However, since the charge carriers are confined to their respective phase, only charge carriers generated in domains that are connected to their respective electrode can be harvested.

The efficiency of the devices is, therefore, among others dependent on three factors: (1) exciton diffusion, (2) exciton dissociation, and (3) charge carrier collection. In order to dissociate, excitons must reach a material interface within their lifetime. This process occurs with high probability when the exciton diffusion length is large compared to the substrate temperature dependent domain size of the material on which the exciton is generated (here, mainly DCV5T-Me). The dissociation rate of the exciton is assumed to be independent of the morphology and, therefore, sample independent. The third important factor our model must describe is the degree of connectivity of the different material domains.

Considering the exciton diffusion process, the RT sample shown in Figure 3 should have a higher internal quantum efficiency in comparison to the 80°C sample shown in Figure 4, which, however, contradicts the experimental findings. On the other hand, small domains, as visible in Figure 3, can lead to island formation, which would not only reduce the

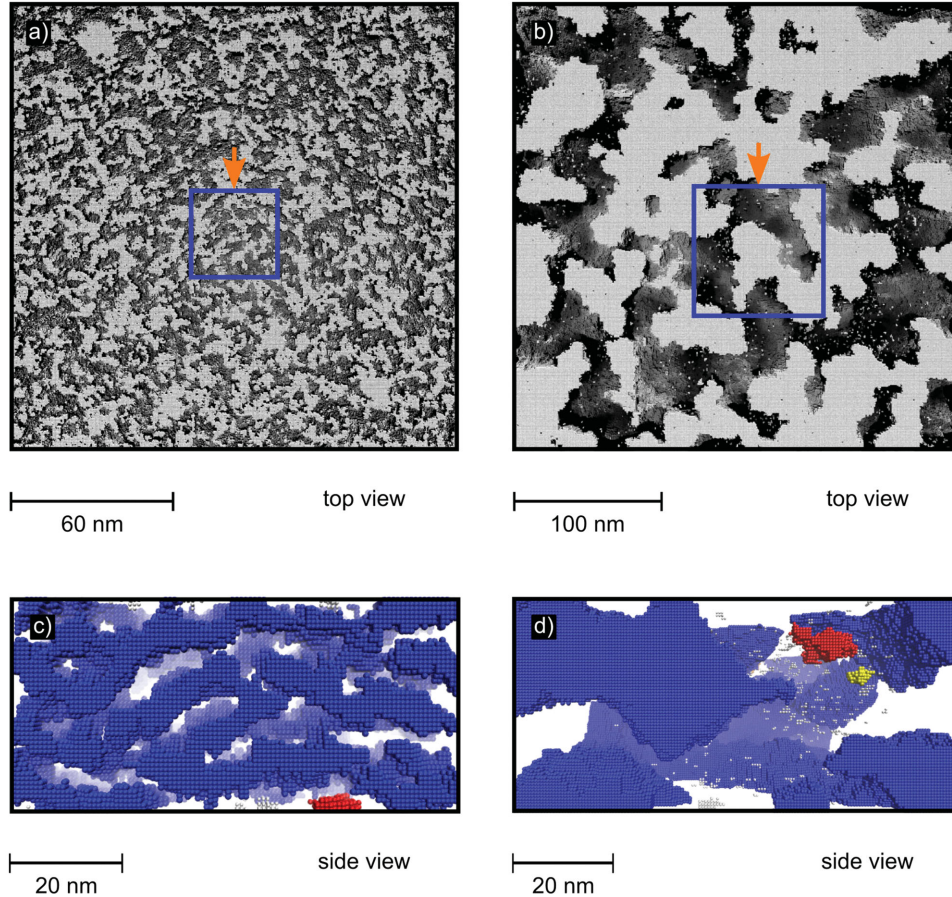


Figure 7. a,b) Top and side views on the 3D DCV-5T-Me (colored):C₆₀ (transparent) microstructure generated by the described MC simulated annealing scheme based on STEM images (Figures 3c and 4c). Part a) shows the simulated morphology of the RT sample and b) of the 80 °C sample. Parts c) and d) show representative vertical slices of the morphologies viewed from the arrow direction for the RT and the 80 °C morphology, respectively. Connected domains are drawn in the same color.

connectivity of material domains, but also facilitate charge carrier recombination, hereby counterbalancing an increased internal quantum efficiency by a worsened charge carrier collection efficiency.

In order to quantify the interplay between domain size and island formation, we generate 3D morphologies based on the STEM-EDX data for the RT and the $T_{\text{sub}} = 80$ °C samples and estimate the exciton and charge mobility in both samples. We do not consider the $T_{\text{sub}} = 140$ °C sample in the simulations as the layer is not entirely closed.

2.3.1. Mesoscale Monte Carlo Simulations

To generate 3D morphologies, we applied a Monte Carlo (MC) simulated annealing method (see the Experimental section) based on 2D STEM-EDX data.^[28] We utilized a heuristic model using the sulfur-sensitive images shown in Figures 3c and 4c, to extract the relative amount of DCV5T-Me in the layer below every pixel of the STEM-EDX image. Afterwards, we generated 3D morphologies that have an identical out-of-plane-projection of the DCV5T-Me content as the STEM-EDX data. Representative illustrations of the morphologies with realistic domain

sizes and interconnectivity in all 3 dimensions are shown in **Figure 7**.

Based on these morphologies, we compute the fraction of voxels in each material that are connected to their respective electrode. In agreement with visual inspection, we find the 80 °C sample to consist of essentially two interpenetrating, singly connected C₆₀ and DCV5T-Me domains that percolate through the entire sample. Surprisingly, the connectivity of the RT sample is equally good, despite its apparent bulk-interface roughness of the domains in the volume. At both substrate temperatures, >99% of the voxels in both domains are connected to the electrodes. This is in agreement with percolation theory, as the volume fraction of the two material components is larger than the percolation threshold of 0.10–0.31, depending on the degree of connectivity.^[29,30] The consequence of this finding is depicted in the side views shown in Figure 7c,d, where the color represents the connectivity of material domains. It is visible that almost all domains are interconnected with each other and build up a complete percolation network (marked in blue). This result explains the observation of similar currents at high negative voltages in Figure 2a. Under these conditions, almost all charge carriers with a connection to the electrodes are extracted with negligible recombination losses and thus, only exciton

separation and material connectivity play a role. An experimentally accessible parameter related to the domain size is the interface area, which we estimated above using sEQE measurements. From the simulated 3D morphology, we derive an interface area per volume in the 80 °C sample which is around 70% smaller than the interface area per volume in the RT sample. This decrease in interface area is in agreement with the sEQE measurement, although the experimental DCV5T-Me:C₆₀ bulk-interface roughness cannot be resolved with the finite voxel size in the simulations.

Based on the simulated 3D morphologies, we compute the mean distance an exciton has to travel to reach an interface. The distribution of distances to the interface (see Figure S4 in the Supporting Information) results in an average equivalent sphere radius of $R_{RT} = 3.1$ nm and 2.8 nm for C₆₀ and DCV5T-Me domains, respectively. For the device prepared at $T_{sub} = 80$ °C, we obtain $R_{80°C} = 10.6$ nm and 9.8 nm for C₆₀ and DCV5T-Me, respectively. These average equivalent sphere radii are in good agreement with the 2D images in Figures 3 and Figure 4c. Even though the equivalent sphere radius in the 80 °C sample is ≈ 10 nm, 83% of the excitons generated are within 4 nm from a donor-acceptor interface. Those values demonstrate that the phase separation at this substrate temperature is just favorably to avoid losses due to exciton recombination, as it is still in the range of estimated values of the exciton diffusion length for this material class (9 ± 3 nm for the DCV6T derivative).^[31]

2.3.2. Microscopic Simulations

In order to understand why the RT sample has a smaller EQE than the 80 °C sample, we next consider the influence of the microscopic material composition on the charge carrier mobility. It is well known that the most significant factor affecting the zero-field mobility of charge carriers in disordered organic semiconductors is the width of the distribution of site energies σ in the system.^[32–35] In principle, there are two sources for energy differences of charge carriers on different sites: (1) differences of the molecular geometry and (2) polarization effects. As both C₆₀ and DCV5T-Me are relatively rigid, the energy disorder mainly arises from electrostatic interactions between the molecules at different sites and their environment.^[36] In order to estimate the energetic disorder as a function of the local material composition, we investigate the strength of polarization effects and their influence on the local energy levels in mixed and pristine material domains. The mixed material domains represent highly disordered material regions in close proximity to the heterointerface which are mainly found in the RT sample. To account for this interface-disorder effect, we generate atomically resolved models for pure C₆₀ and mixed DCV5T-Me:C₆₀ morphologies, representative for the small domains in the RT sample, using a force-field based MC simulated annealing protocol.^[37] The morphologies contain 700 molecules each and are periodically extended in x - and y -direction in order to obtain an electrostatic bulk embedding.

Figure 8 shows the on-site energetic disorder distribution of pure C₆₀ (Figure 8c) and mixed DCV5T-Me:C₆₀ domains (Figure 8d), which correspond to the limiting cases of large,

relatively pure domains in the 80 °C sample and strongly mixed domains in the RT sample. The width of this distribution is closely related to the local density of states and is calculated using the Quantum Patch method.^[38] We find that the width of electrostatic energetic disorder in the pristine C₆₀ system is 8 meV for electrons and 3 meV for holes, respectively. Combined with thermal fluctuations of ≈ 25 meV, we obtain values of ≈ 26 meV which is commensurate with literature data for crystalline organic semiconductors.^[39] In the mixed morphology shown in Figure 8b, the energy disorder of C₆₀ molecules (see Figure 8d) is drastically increased to 158 meV for electrons and 164 meV for holes. This order-of-magnitude increase is caused by the random orientation distribution of DCV5T-Me molecules with respect to the C₆₀ molecules. The intrinsic electrostatic dipole moment of the DCV5T-Me (1.0 Debye) generates a very different electrostatic environment for each C₆₀ molecule, which shifts their respective energy levels. As a result, we obtain a two to three orders of magnitude increase in charge carrier mobility in pure domains of the 80 °C, compared to the mixed RT sample domains (see the Supporting Information for details). As the exciton diffusion coefficient and the exciton diffusion length are exponentially dependent on the energy disorder, we expect a similar effect for excitons, which would largely overcompensate for the increased domain size at the $T_{sub} = 80$ °C sample.^[35] Note that the size of the dipole moment will barely affect the exciton mobility in pristine DCV5T-Me domains as in the 80 °C sample, as these are expected to be highly ordered and, thus, have an energy disorder similar to the low values computed for C₆₀ above.^[36]

3. Discussion

We are able to explain the origins for the improved performance of the 80 °C sample, combining the experimental findings from OSC and morphology characterization with the computational results. Starting from exciton generation, we find a decreased direct absorption into the CT state due to a declined interfacial area in the 80 °C sample compared to the RT sample. Nonetheless, this effect plays only a minor role as most of the absorbed photons generate bound Frenkel type excitons in the absorber.

These excitons have to reach a material interface within their lifetime. Our microstructural analysis yields an increased domain size in the 80 °C sample resulting in two to three times larger average distances (≈ 10 nm) to the nearest donor-acceptor interface compared to the RT sample. This is still within the limits of typical exciton diffusion lengths of 5–40 nm and matches the value for DCV-6T (9 ± 3 nm).^[31,40–42] Therefore, we expect that the fraction of excitons reaching a material interface and being dissociated into electron-hole pairs is not reduced for the sample prepared at 80 °C.

The high current density compared to the RT sample in the j - V curve for negative voltages confirms this experimentally. As the external electric field does not influence the diffusion process of a neutral exciton, this current density reflects the total amount of electrons and holes being generated in the sample and extracted due to the high field strength.

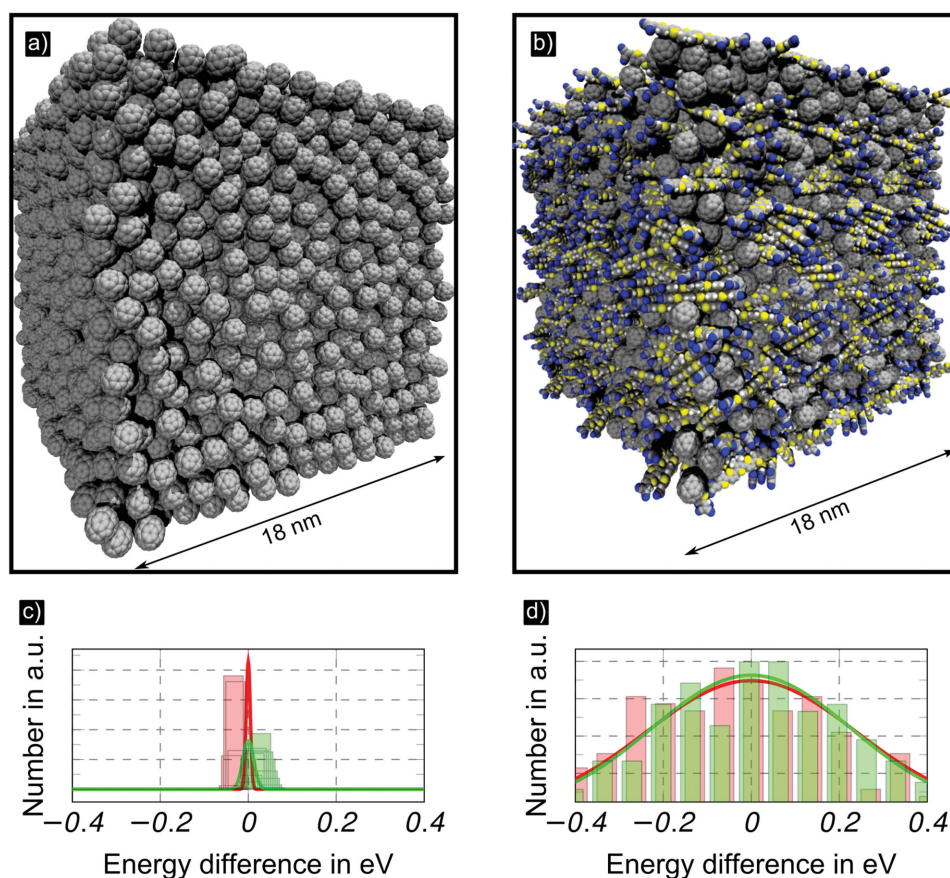


Figure 8. Atomistic morphologies of a) pure C_{60} and b) mixed DCV5T-Me: C_{60} morphologies. Parts c) and d) show the C_{60} on-site energy differences around the HOMO/LUMO (red/green bars and lines) of C_{60} for the morphologies shown in (a) and (b). The solid lines represent Gaussian fits. The width of these distributions is the energetic disorder and determines the electron and hole mobilities.

We furthermore find in the analysis of the 3D domain structure that the connectivity of the percolation network is equally good in the 80 °C sample and in the RT sample. The interpenetrating domain network comprises more than 99% of the molecules in the bulk-heterojunction, providing well connected transport paths for the majority of charge carriers towards their respective transport layers.

This finding depends only on the volume fraction of the two materials. 3D percolation theory for different connectivity models predicts infinite percolation paths without significant island formation for material fractions larger than 12%–30% of the material volume.^[29,30] For most BHJs used in OSC, both materials have a significantly larger fraction than these values. Therefore, this result can be generalized: Carrier trapping due to the formation of small isolated islands will only play a role for extreme volume ratios and is usually independent of the domain sizes in the BHJ. Note that despite an island-free percolation network, dead-end formation of material domains in field direction may lead to charge traps.

Due to the independence of the percolation network on the domain sizes, we emphasize another parameter playing an important role for charge transport, namely the energetic disorder. Mixed material domains in close proximity to a disordered material interface and other deviations from relatively ordered pure material domains lead to a strong decrease of

the charge carrier mobility. This is particularly crucial in the case of material combinations where at least one material has an intrinsic dipole moment, such as DCV5T-Me, leading to energetic disorder contributions from polarization effects. Improved exciton mobility in the more pristine domains of the 80 °C sample increases the exciton diffusion lengths and overcompensates the increased distances to the next material interface. At the same time, enhanced charge transport properties lead to a faster charge extraction and to a lower series resistance yielding an improved fill factor.

These findings are well supported by both theory and experiment and conclusively explain the improved performance of the 80 °C sample. Simultaneously, they give design rules for the development of more efficient organic solar cells. One important factor determining the device efficiency is the formation of pristine and, in the case of materials which have an intrinsic dipole moment, ordered material domains. As shown in this study, this can be achieved e.g., by tuning the substrate temperature during deposition of the bulk-heterojunction.

4. Summary

We characterized the absorber layer morphology of the highly efficient donor–acceptor couple DCV5T-Me: C_{60} on various

length scales. To obtain comprehensive insight into the relationship between the PCE of organic solar cells and the deposition temperature of the absorber layer, we employed methods such as j - V curves, STEM-EDX, (s)EQE measurements, and mesoscopic and microscopic simulations.

STEM-EDX measurements reveal a well-intermingled morphology of the RT (PCE = 4.5%) sample with very small structures. Increasing T_{sub} to 80 °C (PCE = 6.8%) results in a small-scale phase separation between DCV5T-Me and C_{60} , where both materials form relatively pure, well-connected interpenetrating networks. Due to the enhanced phase separation between DCV5T-Me and C_{60} at $T_{\text{sub}} = 80^\circ\text{C}$, we observe a reduction of the interfacial area between donor and acceptor in sEQE measurements. The strongly decreased PCE of solar cell deposited at $T_{\text{sub}} = 140^\circ\text{C}$ is explained by the reduced EQE as compared to the sample deposited at $T_{\text{sub}} = 80^\circ\text{C}$. The reduction of EQE is clarified by STEM-EDX investigations, where an incomplete surface coverage along with the strong demixing of DCV5T-Me and C_{60} is observed. Another contribution to the breakdown of the EQE originates from the significantly reduced interfacial area between DCV5T-Me and C_{60} as compared to the solar cells deposited at lower substrate temperatures.

We perform simulations of the mesoscale morphology and the microscopic charge and exciton transport properties. We find that domain connectivity and percolation properties are independent of the domain size of the bulk-heterojunction. Our analysis of the energetic disorder points to a drastic effect of material mixing on the exciton mobility. Especially mixtures with materials with an intrinsic dipole moment, e.g., DCV5T-Me, charge carrier, and exciton mobility is severely diminished. The effect of increased charge carrier mobility due to demixing of materials plays the most dominant role in the improved performance of the solar cell deposited at a substrate temperature of 80 °C. This effect overrules the effect of increased distances which the excitons have to overcome in order to reach an interface.

5. Experimental Section

Device Fabrication and Characterization: The samples were produced in a vacuum chamber (K. J. Lesker, UK) with a base pressure of 10^{-8} mbar. The devices were prepared on prestructured indium tin oxide (ITO) coated glass (Thin film devices, USA, 90 nm thin, $26 \Omega\text{sq}^{-1}$, 84% transparency). After the production, the cells were encapsulated under a nitrogen atmosphere with epoxy glue and a cover glass. The area of the solar cells is 6.44 mm^2 and is defined by the geometrical intersections of the indium tin oxide bottom electrode and the aluminum top electrode.

As electron transport layer C_{60} (CreaPhys, Dresden, Germany, density 1.63 gcm^{-3}) was n-doped with tetrakis(1,3,4,6,7,8-hexahydro-2H-pyrimido[1,2-a]pyrimidinato) ditungsten (II) ($W_2(\text{hpp})_4$, Novaled, Germany). The hole transport layers of the devices start with an intrinsic layer of 9,9-bis[4-(*N,N*-bis-biphenyl-4-yl-amino)phenyl]-9H-fluorene (BPAPF, LumTec, Taiwan) to prevent recombination between electrons from the acceptor phase with free holes in the doped transport layers. Afterward, two p-doped hole transport layers were deposited. First, BPAPF was p-doped with NDP9 (Novaled, Dresden, Germany) and a layer of *N,N'*-(Diphenyl-*N,N'*-bis(9,9-dimethyl-fluoren-2-yl))-benzidine (BF-DPB, Synthon, Bitterfeld, Germany) also doped with NDP9. Next, an additional 1 nm pure NDP9 layer increased the doping concentration at the aluminum interface and guarantees an Ohmic contact.

The donor 2,2'-((3'',4''-dimethyl-[2,2':5',2'':5'',2''':5''',2''''-quinque-thiophene]-5,5''''-diyl) bis(methanylylidene)) dimalononitrile (DCV5T-Me, Synthon Chemicals, Bitterfeld, Germany, density 1.3 gcm^{-3} , evaporation rate 0.1 \AA s^{-1}) was blended with C_{60} (evaporation rate 0.05 \AA s^{-1}). The bilayer device was manufactured in the following layer sequence: ITO | 15 nm C_{60} | 6 nm DCV5T-Me | 5 nm BPAPF | 40 nm p-BPAPF (10 wt% NDP9) | 1 nm NDP9 | 100 nm Al.

The encapsulated devices were measured under a mismatch corrected illumination of the solar simulator 16S-003-300-AM1.5 (Solar Light Co., USA). The intensity was monitored with a Hamamatsu S1337 silicon photodiode (Herrsching am Ammersee, Germany). The EQE measurements were performed with a custom-made set-up consisting of a lamp (Oriol Xe Arc-Lamp Apex Illuminator), a monochromator (Cornerstone 260 1/4m, Newport, Darmstadt, Germany), a chopper, and a Lock-in amplifier (SR 7265, Signal Recovery, Oak Ridge, USA).

Sensitive EQE: In order to resolve the absorbance spectrum $A(E)$, revealing the interfacial CT transitions, the sEQE was normalized to the absorbance obtained via a measurement of the reflectance (R), i.e., $A = 1 - R$. More precisely, the sEQE spectra was rescaled by a constant c to the absorbance ($A = c \times \text{sEQE}$) in the high-energy region around 2.2 eV.

Light from a quartz halogen lamp was coupled into a monochromator (Cornerstone 260 1/4m, Newport, Darmstadt, Germany) and chopped at a frequency of 139 Hz. The subsequently monochromatic light was focused onto the photovoltaic device. The resulting photocurrent was amplified with a current pre-amplifier (DHPCA-100, FEMTO Messtechnik GmbH, Berlin, Germany) before feeding the signal to a lock-in amplifier (7280 DSP, Signal Recovery, Oak Ridge, USA). Pre-amplifier sensitivity ($10^5 - 10^6 \text{ A/V}$) and lock-in time constant (1 s) were increased in order to enable measuring a signal at low photon energies and, thus, low photocurrents. The EQE was determined by dividing the output electron flux per incident photon of the photovoltaic device by the incident photon flux, as measured by a calibrated silicon (FDS100-CAL, Thorlabs, Munich, Germany) and indium-gallium-arsenide-photodiode (FGA21-CAL, Thorlabs, Munich, Germany).

Morphological Characterization: 40 nm thin absorber layers were deposited at the above specified substrate temperatures on 30 nm thin Si_3N_4 TEM-windows (Silson Ltd, UK). The measurements were performed at a probe C_s corrected STEM (FEI Titan Cubed G2 60–300) equipped with a ChemiSTEM EDX system operated at 60 kV optimized for minimal electron damage to the samples.^[43,44] All recorded images have a size of $512 \times 512 \text{ pixel}^2$ with a dwell time of 50 μs per pixel. All images were acquired with enabled drift-correction scanning multiple times over the same area. The image specific parameters are: RT sample: probe current 3 nA, acquisition time 5779 s. For the 80 °C sample: probe current 600 pA, acquisition time 4500 s. And for the 140 °C sample: probe current 2.8 nA, acquisition time 6180 s. To determine the elemental contribution, the Cliff-Lorimer method was implemented in Bruker's Esprit software.^[21]

Monte Carlo Modeling: Initially, a 3D array was randomly filled with DCV5T-Me and C_{60} voxels according to the 2D projection, measured by STEM. In the next step, positive/negative interaction energies were assigned to boundaries between different/equal voxel types. During the simulated annealing procedure, steps were performed, where two vertically connected voxels could exchange their positions. This ensured that the vertical projection, meaning the STEM-EDX input data, remained unchanged during the simulation. Moreover, steps were allowed according to the Metropolis Monte Carlo criterion: all steps leading to a lower total energy of the system were accepted, whereas steps which increased the total energy were only accepted with a probability determined by the Boltzmann factor $\exp(-\Delta E/k_B T)$ with a certain temperature T and the energy gain ΔE due to the Monte Carlo step. Further, details can be found in the Supporting Information.

Microscopic Simulations: All DFT calculations for the energy disorder and the electronic couplings within the Quantum Patch method were performed using TURBOMOLE with a hybrid B3-LYP functional and a def2-SV(P) basis set.^[33,45] Reorganization energies and dipole moments were calculated using a B3-LYP functional and a def2-TZVP basis-set.

Supporting Information

Supporting Information is available from the Wiley Online Library or from the author.

Acknowledgements

T.M. and P.F. contributed equally to this work. The authors acknowledge funding by the BMBF in the framework of the project MEDOS (03EK3503A) and the InnoProfile project "organische pin Bauelemente 2.2" (03IPT602X). Moreover, the authors thank Sven Kunze, Daniel Schütze, Christoph Hauenstein, and the IAPP Lesker team for their kind assistance. The research leading to these results received funding from the European Union Seventh Framework Programme under Grant Agreement No. 312483 – ESTEEM2 (Integrated Infrastructure Initiative–I3). The authors acknowledge funding by the Helmholtz program "Science and Technology of Nanosystems" (STN), the STN-DFG project MODEOLED, and the Carl-Zeiss Foundation for funding the project "Multiskalen Modellierung elektronischer Eigenschaften von Materialien in der organischen Elektronik." The calculations were performed on the computational resource ForHLR Phase I funded by the Ministry of Science, Research and the Arts Baden-Württemberg and DFG ("Deutsche Forschungsgemeinschaft").

- [1] C. W. Tang, *Appl. Phys. Lett.* **1986**, *48*, 183.
- [2] A. Henemann, *Renew. Energy Focus* **2008**, *9*, 14.
- [3] Q. Zhang, B. Kan, F. Liu, G. Long, X. Wan, X. Chen, Y. Zuo, W. Ni, H. Zhang, M. Li, Z. Hu, F. Huang, Y. Cao, Z. Liang, M. Zhang, T. P. Russell, Y. Chen, *Nat. Photonics* **2014**, *9*, 35.
- [4] Heliatek, Heliatek consolidates its technology leadership by establishing a new world record for organic solar technology with a cell efficiency of 12%, **2013**.
- [5] M. Hiramoto, H. Fujiwara, M. Yokoyama, *Appl. Phys. Lett.* **1991**, *58*, 1062.
- [6] G. Yu, J. Gao, J. C. Hummelen, F. Wudl, A. J. Heeger, *Science*. **1995**, *270*, 1789.
- [7] W. Ma, J. R. Tumbleston, M. Wang, E. Gann, F. Huang, H. Ade, *Adv. Energy Mater.* **2013**, *3*, 864.
- [8] J. R. Tumbleston, B. A. Collins, L. Yang, A. C. Stuart, E. Gann, W. Ma, W. You, H. Ade, *Nat. Photonics* **2014**, *8*, 385.
- [9] T. Mönch, P. Guttmann, J. Murawski, C. Elschner, M. Riede, L. Müller-Meskamp, K. Leo, *Org. Electron.* **2013**, *14*, 2777.
- [10] D. Wynands, M. Levichkova, K. Leo, C. Urich, G. Schwartz, D. Hildebrandt, M. Pfeiffer, M. Riede, *Appl. Phys. Lett.* **2010**, *97*.
- [11] K. Schulze, C. Urich, R. Schüppel, K. Leo, M. Pfeiffer, E. Brier, E. Reinold, P. Bäuerle, *Adv. Mater.* **2006**, *18*, 2872.
- [12] C. Koerner, C. Elschner, N. C. Miller, R. Fitzner, F. Selzer, E. Reinold, P. Bäuerle, M. F. Toney, M. D. McGehee, K. Leo, M. Riede, *Org. Electron.* **2012**, *13*, 623.
- [13] B. Maennig, D. Gebeyehu, P. Simon, F. Kozlowski, A. Werner, F. Li, S. Grundmann, S. Sonntag, M. Koch, K. Leo, M. Pfeiffer, H. Hoppe, D. Meissner, N. S. Sariciftci, I. Riedel, V. Dyakonov, J. Parisi, J. Drechsel, *Appl. Phys. Mater. Sci. Process.* **2004**, *79*, 1.
- [14] C. Poelking, M. Tietze, C. Elschner, S. Olthof, D. Hertel, B. Baumeier, F. Würthner, K. Meerholz, K. Leo, D. Andrienko, *Nat. Mater.* **2014**, *14*, 434.
- [15] R. Fitzner, E. Reinold, A. Mishra, E. Mena-Osteritz, H. Ziehle, C. Körner, K. Leo, M. Riede, M. Weil, O. Tsaryova, A. Weiß, C. Urich, M. Pfeiffer, P. Bäuerle, *Adv. Funct. Mater.* **2011**, *21*, 897.
- [16] H. Ziehle, L. Burtone, C. Koerner, R. Fitzner, E. Reinold, P. Bäuerle, K. Leo, M. Riede, *Org. Electron.* **2011**, *12*, 2258.
- [17] Z. Yang, M. Corso, R. Robles, C. Lotze, R. Fitzner, E. Mena-Osteritz, P. Bäuerle, K. J. Franke, J. I. Pascual, *ACS Nano* **2014**, *8*, 10715.
- [18] H. W. Kroto, J. R. Heath, S. C. O'Brien, R. F. Curl, R. E. Smalley, *Nature* **1985**, *318*, 162.
- [19] R. Schueppel, K. Schmidt, C. Urich, K. Schulze, D. Wynands, J. L. Brédas, E. Brier, E. Reinold, H.-B. Bu, P. Bäuerle, B. Maennig, M. Pfeiffer, K. Leo, *Phys. Rev. B* **2008**, *77*, 085311.
- [20] R. Meerheim, C. Körner, K. Leo, *Appl. Phys. Lett.* **2014**, *105*, 063306.
- [21] D. B. Williams, C. B. Carter, *Transmission Electron Microscopy: A Textbook for Materials Science*, Vol. 1, Springer, **2009**.
- [22] J. B. Gilchrist, T. H. Bases-Fisher, S. C. Chang, F. Scheltens, D. W. McComb, S. Heutz, *Adv. Funct. Mater.* **2014**, *24*, 6473.
- [23] M. Pfannmöller, H. Flügge, G. Benner, I. Wacker, C. Sommer, M. Hanselmann, S. Schmale, H. Schmidt, F. A. Hamprecht, T. Rabe, W. Kowalsky, R. R. Schröder, *Nano Lett.* **2011**, *11*, 3099.
- [24] E. Buchaca-Domingo, K. Vandewal, Z. Fei, S. E. Watkins, F. H. Scholes, J. H. Bannock, J. C. de Mello, L. J. Richter, D. M. DeLongchamp, A. Amassian, M. Heeney, A. Salleo, N. Stingelin, *J. Am. Chem. Soc.* **2015**, *137*, 5256.
- [25] S. J. Pennycook, *Ultramicroscopy* **1989**, *30*, 58.
- [26] F. Maier-Flaig, C. Kübel, J. Rinck, T. Bocksrocker, T. Scherer, R. Prang, A. K. Powell, G. A. Ozin, U. Lemmer, *Nano Lett.* **2013**, *13*, 3539.
- [27] J. Wen, D. J. Miller, W. Chen, T. Xu, L. Yu, S. B. Darling, N. J. Zaluzec, *Microsc. Microanal.* **2014**, *20*, 1507.
- [28] P. K. Watkins, A. B. Walker, G. L. B. Verschoor, *Nano Lett.* **2005**, *5*, 1814.
- [29] J. Wang, Z. Zhou, W. Zhang, T. M. Geroni, Y. Deng, *Phys. Rev. E* **2013**, *87*, 052107.
- [30] K. Malarz, *Phys. Rev. E* **2015**, *91*, 054509.
- [31] D. Wynands, B. Männig, M. Riede, K. Leo, E. Brier, E. Reinold, P. Bäuerle, *J. Appl. Phys.* **2009**, *106*, 043301.
- [32] H. Bässler, *Phys. Status Solidi B* **1993**, *175*, 15.
- [33] P. Friederich, V. Meded, F. Symalla, M. Elstner, W. Wenzel, *J. Chem. Theory Comput.* **2015**, *11*, 560.
- [34] V. Rodin, F. Symalla, V. Meded, P. Friederich, D. Danilov, A. Poschlad, G. Nelles, F. von Wrochem, W. Wenzel, *Phys. Rev. B* **2015**, *91*, 155203.
- [35] D. L. Huber, *J. Chem. Phys.* **1983**, *78*, 2530.
- [36] R. Fitzner, E. Mena-Osteritz, A. Mishra, G. Schulz, E. Reinold, M. Weil, C. Körner, H. Ziehle, C. Elschner, K. Leo, M. Riede, M. Pfeiffer, C. Urich, P. Bäuerle, *J. Am. Chem. Soc.* **2012**, *134*, 11064.
- [37] T. Neumann, D. Danilov, C. Lennartz, W. Wenzel, *J. Comput. Chem.* **2013**, *34*, 2716.
- [38] P. Friederich, F. Symalla, V. Meded, T. Neumann, W. Wenzel, *J. Chem. Theory Comput.* **2014**, *10*, 3720.
- [39] V. Coropceanu, J. Cornil, D. A. da Silva Filho, Y. Olivier, R. Silbey, J.-L. Brédas, *Chem. Rev.* **2007**, *107*, 926.
- [40] S.-B. Rim, R. F. Fink, J. C. Schöneboom, P. Erk, P. Peumans, *Appl. Phys. Lett.* **2007**, *91*, 173504.
- [41] P. Peumans, A. Yakimov, S. R. Forrest, *J. Appl. Phys.* **2003**, *93*, 3693.
- [42] R. R. Lunt, J. B. Benziger, S. R. Forrest, *Adv. Mater.* **2010**, *22*, 1233.
- [43] R. F. Egerton, P. Li, M. Malac, *Micron* **2004**, *35*, 399.
- [44] O. L. Krivanek, N. Dellby, M. F. Murfitt, M. F. Chisholm, T. J. Pennycook, K. Suenaga, V. Nicolosi, *Ultramicroscopy* **2010**, *110*, 935.
- [45] R. Ahlrichs, M. Bär, M. Häser, H. Horn, C. Kölmel, *Chem. Phys. Lett.* **1989**, *162*, 165.